Comparative analysis of process-induced strain glass states in austenitic and martensitic NiTi shape memory alloy plates

Neha S. John[1]*, Bailey Ashmore[1], Michael T. Wall[1], Robert W. Wheeler[1], Marcus L. Young[1] and Anit K. Giri[2]

[1]Department of Material Sciences and Engineering, University of North Texas, Denton, TX, United States, [2]Army Research Directorate, DEVCOM Army Research Laboratory, APG, Adelphi, MD, United States

Strain glass alloys (SGAs) are metallic alloys with glassy martensitic nanodomains within a crystalline material that occur from compositionally or processing-induced strain. SGAs originate from shape memory alloys (SMAs) and exhibit similar shape memory properties and high actuation densities. The transition from SMA to SGA is relatively unexplored, and although there are similarities to amorphous SMAs and cold-worked SMAs, SGAs should be distinguished as a separate grouping. The transition occurs by interrupting the long-range martensitic order, which in turn disrupts the martensitic transformation, resulting in short-range martensitic order. A glassy martensitic phase is produced that exhibits enhanced structural and load-bearing abilities, functional stresses, and recoverability. In this study, the transformation from SMA to SGA is explored in two common commercially available SMAs, $Ni_{49.5}Ti_{50.5}$ and $Ni_{50.8}Ti_{49.2}$ (at. %), to compare martensitic versus austenitic SGAs, respectively. SMA plates were cold worked in 5% increments until a strain glass transition occurred. Characterizations of the samples at various stages of cold work were examined via differential scanning calorimetry (DSC), Vickers hardness, transmission electron microscopy (TEM), and synchrotron radiation X-ray diffraction (SR-XRD). Some prominent characteristics between the two plates, such as enthalpy peaks, twin size reduction, and crystallographic structure, were examined and compared to improve the understanding of the SMA to SGA transition.

KEYWORDS

strain glass alloys, process-induced strain, shape memory alloy, cold work, martensitic transformation

Introduction

The discovery of SMAs was monumental, affecting multiple industries such as aerospace, automotive, biomedical, and civil engineering (Stoeckel, 1990; Hartl and Lagoudas, 2007; Kapoor, 2017). This material group has extensively impacted the fields of active and elastocaloric materials, due to desired thermal and mechanical properties, cyclical abilities, while being lightweight and elementally diverse. The quintessential characteristics of SMAs are the shape memory effect, martensitic transformation, pseudoelastic effect, and actuation response due to exhibiting high actuation densities (Otsuka and Wayman, 1998; Hartl and Lagoudas, 2008). The shape memory effect is defined

by the recoverability hysteresis that shows the phase transformations that occur from thermal cycling and/or applying load. The martensitic transformation is a sharp single-step transformation that occurs when the material shifts from austenite to twinned martensite. It is a solid–solid, diffusionless transformation resulting from a change in crystal structure but no diffusion of atoms. The pseudoelastic effect is defined by the complete shape recovery that occurs when the material is loaded in the high-temperature austenitic phase. A phase transformation from austenite to martensite occurs when loaded, which appears as additional elasticity, that is, "pseudoelasticity." The material transforms back to the austenite phase upon unloading, allowing for a repeatable and fully recoverable shift between the two phases (Tadaki et al., 1988). While SMAs have been studied extensively (Tadaki et al., 1988; Stoeckel, 1990; Otsuka and Wayman, 1998; Miller and Lagoudas, 2001; Otsuka and Ren, 2005; Hartl and Lagoudas, 2007; Hartl and Lagoudas, 2008; Lobo et al., 2015; Kapoor, 2017; Ko et al., 2021), the effect of restricting the martensitic transformation (B2→B19′ transformation) to nanodomains has remained relatively unexplored. This group of SMAs are called strain glass alloys (SGAs) (Sarkar et al., 2005; Wheeler et al., 2018a).

SGAs are a recently discovered group of active metallic alloys derived from SMAs. Unlike SMAs, SGAs do not show any phase transformation from thermal cycling; however, a phase transformation occurs via mechanical loading (Wheeler et al., 2018a). Some of the improved functional properties of SGAs are operational stresses, dimensional stability, and higher actuation densities (Wheeler et al., 2019). SGAs represent a new method of processing SMAs to obtain desired characteristics with multifunctional properties.

The transformation from SMA to SGA occurs when the martensitic transformation is disrupted, and glass-like martensitic nanodomains are produced via induced strain. The martensitic transformation noticed in SMAs, which is a single-step sharp transition, is replaced by the continuous strain glass transition, along with highly strained austenite (Wheeler et al., 2018b; Wang M. et al., 2022). This disruption can occur by compositionally or processing-induced strain. A precise amount of strain is necessary in both types of SGAs, causing the interruption of the transformation and making the alloy harder. The increase in hardness inhibits the thermal phase transformation and increases the actuation stresses of the alloy, which ultimately increases the work output of the SGA (Wheeler et al., 2018b).

SGAs have been mostly studied in near-equiatomic NiTi systems (Sarkar et al., 2005; Zhang et al., 2010; Qin et al., 2017; Wheeler et al., 2018a; Wheeler et al., 2018b; Bag et al., 2019; Wheeler et al., 2019; Liang et al., 2022). Compositionally induced strain occurs from altering the alloy composition and/or incorporating additional elements to SMAs, causing lattice distortions. These lattice distortions break up the long-range order (LRO) martensitic twins noticed in SMAs and result in short-range order (SRO) martensite that forms amorphous nanodomains (Ren, 2011). Whenever the alloy system is above a critical concentration, the thermal phase transformation is no longer observed. Elemental additions in NiTi-based SMA systems such as Fe (Wang et al., 2010; Hou, 2012), Cu (Hao et al., 2019; Wang W. et al., 2022), Co, Cr, and Mn (Zhou et al., 2010) have also proven to have a strain glass transition at specific concentrations. Most studied SGA systems are compositionally induced (Sarkar et al., 2005; Wang et al., 2010; Zhang et al., 2010; Zhou et al., 2010; Hou, 2012; Qin et al., 2017; Hao et al., 2019; Chen et al., 2020; Xu et al., 2021; Wang W. et al., 2022); however, another method of achieving strain glass states called processing-induced SGAs was recently identified (Wheeler et al., 2018a; Wheeler et al., 2018b; Wheeler et al., 2019; Liang et al., 2022). In compositionally and processing-induced SGAs, strain is introduced into the lattice in the form of atomic size mismatch or dislocations, respectively. As the concentration of these strain-inducing defects increases, the domain size of martensite decreases (Wang M. et al., 2022). When the defect concentration surpasses a critical value, there is a transformation in microstructure from twinned LRO domains to fragmented nanodomains.

This study focuses on processing-induced SGAs, which are produced by introducing dislocations into SMAs via cold working. These dislocations disturb the periodic distribution of atoms, which disrupts the martensitic transformation and causes glassy SRO martensite by finely fragmenting the martensitic twins. For processing-induced SGAs, an initial SMA composition is cold worked in steps, or rolling passes, to the point at which the thermal response is fully suppressed. One unique aspect of processing-induced SGAs, as compared to compositionally induced SGAs, is that the transformation temperatures can remain fixed.

It is important to distinguish processing-induced SGAs from cold-worked SMAs (Miller and Lagoudas, 2001; Khelfaoui and Guénin, 2003; Chang et al., 2017) and amorphous SMAs (Koike et al., 1990; Sergueeva et al., 2003; Peterlechner et al., 2010; Jiang et al., 2013). Cold-working SMAs is a method of hardening the material that is commonly employed for processing and to obtain amorphous NiTi SMAs. While processing-induced SGAs may seem synonymous with cold-worked or amorphous NiTi SMAs, there are key characteristics that distinguish the three groups of alloys. SGAs are comprised of a crystalline matrix with amorphous nanodomains (Wheeler et al., 2018a), while amorphous SMAs are comprised of an amorphous matrix with a nanocrystalline phase (Koike et al., 1990). Generally, the intent with cold-worked SMAs is to create finer grains and introduce some dislocations into the material, which improves the ease of transformation (Miller and Lagoudas, 2001). Cold-worked SMAs tend to still exhibit thermal-phase transformation and recoverability (Chang et al., 2017). In contrast, amorphous SMAs are cold worked with the intent of achieving total SRO and exhibit degraded pseudoelastic behavior and shape memory effect, meaning the alloy shows very low or no recoverability but exhibits an increase in elasticity and strength (Ko et al., 2021). Conversely, SGAs show nearly linear pseudoelastic behavior (Wang et al., 2006). Complete amorphization, or merely cold working the material, is not the aim with processing-induced SGAs. Rather, the aim is to obtain the precise amount of strain required to suppress the thermal phase transformation and provide enhanced mechanical properties. One of the key distinctions of processing-induced SGAs is recognizing when the thermal transformation has been fully suppressed, meaning the martensite has become thoroughly distributed as amorphous nanodomains in a strained austenitic crystalline matrix. Beyond this critical point, the material becomes more amorphous and mechanically brittle, while below this critical point, the material still shows some LRO and only exhibits a strained thermal transformation. The enhanced mechanical properties of SGAs are a result of precisely

controlling the amount of input strain, that is, dislocations worked into the material. The introduction of dislocations makes the material harder to transform, which in turn increases the amount of work generated by the SGA. The purpose and importance of SGAs, as compared to cold-worked and amorphous SMAs, lies in the ability of the material to have shape memory-like behavior with a fully suppressed thermal response and an enhanced mechanical response.

The aim of this study is to investigate and compare the two compositions of the commercially available SMA plates and explore where the SGA transition occurs. This was achieved by cold-working sections of the $Ni_{49.5}Ti_{50.5}$ and $Ni_{50.8}Ti_{49.2}$ (at. %) SMA plates in 5% increments until the thermal response was fully repressed. Differential scanning calorimetry (DSC) was performed on the cold-rolled samples to determine the critical amount of strain necessary to fully suppress the thermal transformation that indicates when a potential SGA has been created. Vickers hardness testing provided an elementary method to determine the heightened resistance to plastic deformation that is characteristic of potential SGAs. Both DSC and Vickers hardness testing served as preliminary characterization techniques to prove a potential SGA was achieved by showing the suppressed thermal transformation and proving an increase in resistance to plastic deformation. Transmission electron microscopy (TEM) and synchrotron radiation X-ray diffraction (SR-XRD) were further performed to determine the strain glass transition for both plates and provide detail regarding the micro- and nano-structural characteristics. This testing allows further elucidation of processing-induced SGAs and their associated properties.

Material selection

SMA plates of $Ni_{49.5}Ti_{50.5}$ (SM495) and $Ni_{50.8}Ti_{49.2}$ (SE508) were supplied by ATI Specialty Alloys & Components. These compositions were specifically investigated for four reasons: a) highly researched; their behavior and properties are well-known, b) commercial availability, c) binary compositions make it easier to isolate the effects of cold work, and d) the presence of different phases result in different properties at room temperature. At room temperature, $Ni_{49.5}Ti_{50.5}$ is fully martensitic, while $Ni_{50.8}Ti_{49.2}$ is fully austenitic.

Although the compositions seem analogous, the 1.3 at. % Ni difference has a large impact on the transformation temperatures and associated properties. The $Ni_{49.5}Ti_{50.5}$ SMA plate is a Ni-lean NiTi composition that is known for its shape memory effect at room temperature, along with being in the martensitic phase. In similar studies by Wheeler et al. (2018a), Wheeler et al. (2018b), and Wheeler et al. (2019), a $Ni_{49.5}Ti_{50.5}$ SMA rod was cold worked to discover that the processing-induced strain glass state in this material occurred at a 44% thickness reduction. An in-depth analysis of the same $Ni_{49.5}Ti_{50.5}$ material via SR-XRD characterization was conducted by Ashmore et al. (2023). The $Ni_{50.8}Ti_{49.2}$ SMA plate is a Ni-rich NiTi composition that is known for its pseudoelasticity at room temperature as well as being in the austenitic phase.

The objective of this research is to further identify the critical defect concentration to induce a strain glass transition in existing SMA NiTi systems. Studies have shown that both $Ni_{49.5}Ti_{50.5}$ (Wheeler et al., 2018a; Wheeler et al., 2018b; Wheeler et al., 2019; Ashmore et al., 2023) and $Ni_{50.8}Ti_{49.2}$ (Liang et al., 2022) have a strain glass transition. These two SMA plates were chosen for this study to further investigate and compare the effects of disrupting the martensitic transformation on the material that starts in either martensite or austenite at room temperature.
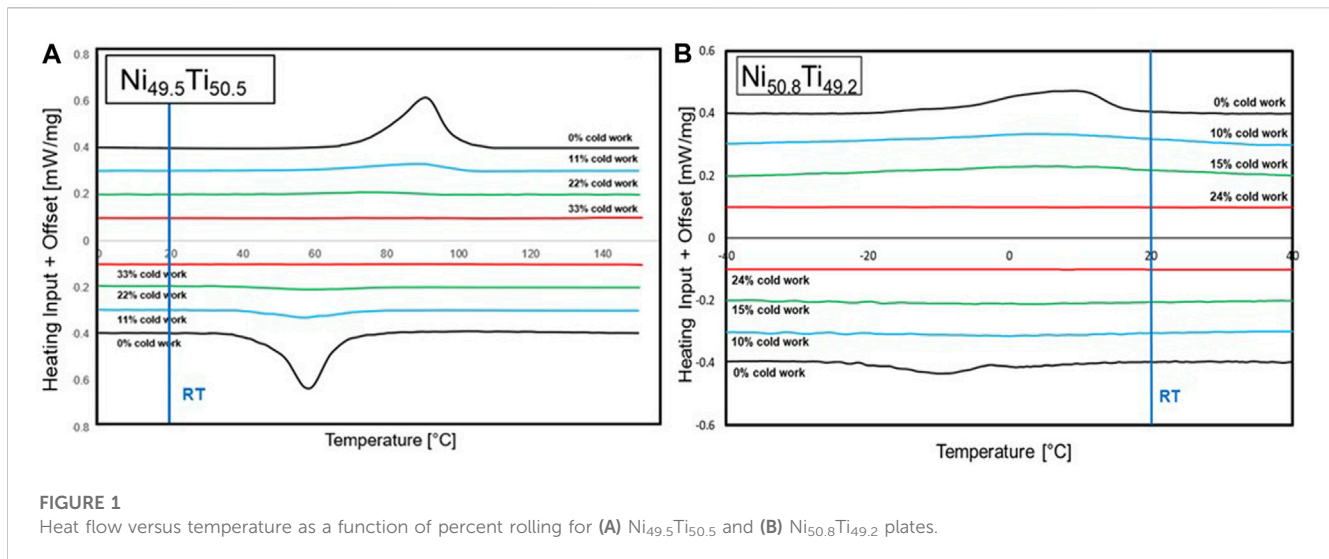
Experimental methods

The as-received SMA state (0% cold rolled) was fully characterized for comparison with SGA samples and to estimate the amount of cold rolling necessary to suppress the martensitic transformation.

Rolling in linear passes at room temperature was conducted using a Durston Rolling Mill to ensure a precisely controlled amount of input strain. DSC samples were prepared by cutting a small sample section, weighing between 14 mg and 25 mg, with a low-speed diamond saw. The sample was then placed and sealed in an Al crucible before being programmed and tested using a Netzsch DSC 204 F1 Phoenix. The samples were tested using a temperature profile between −100°C and 200°C at a heating rate of 10°C/min. The process of cold rolling in 5% increments and performing DSC continued in steps until the transformation temperatures were constant, meaning there was no associated enthalpy peak detected for both $Ni_{49.5}Ti_{50.5}$ and $Ni_{50.8}Ti_{49.2}$. The previous 5% increment samples were then revisited and rolled in smaller 1% increments to verify exactly when the SGA state was reached, that is, the precise amount of rolling required to completely remove the thermal response, or enthalpy peaks. Further characterization was employed and necessary to prove a strain glass transition.

Vickers hardness was performed to test the alloy's ability to resist plastic deformation as it was processed. Samples were prepared for each 5% increment by cold mounting and polishing to a mirror finish. Ten indents, arranged in a 5×2 array with 0.5 mm spacing, were programmed using an automatic Vickers hardness tester at 0.5 HV. The resulting hardness values were averaged for each increment and graphed.

TEM was performed to visualize the nanostructure and nanodomains between the as-received SMA and cold-rolled SGA states. TEM samples were prepared using a focused ion beam (FIB) lift-out technique with an FEI Nova FIB/SEM. TEM was performed using an FEI Tecnai G2 F20S-Twin S/TEM operating at 200 keV. High-resolution TEM micrographs were collected in the high-angle annular dark field and bright-field Z-contrast configuration.

The as-received state, two intermediate cold-rolled states, and the potential SGA state were further characterized using SR-XRD to collect wide-angle X-ray scattering (WAXS) diffraction patterns and d-spacing plots. High-energy SR-XRD measurements were collected at the Sector 6-ID-D beamline of the Advanced Photon Source (APS) at Argonne National Laboratories. A beam energy of 60 keV and a beam size of 400×200 μm^2 were used. Samples were aligned with the long axis of the sample in the vertical direction normal to the beam. Each *ex situ* diffraction pattern represents 100 summed, 0.1 s exposures, for a total of 10 s per diffraction image. Full Debye–Scherrer diffraction rings were collected using a PerkinElmer amorphous Si detector at a distance of 36 cm from the sample and calibrated using a CeO_2 standard.

FIGURE 1
Heat flow versus temperature as a function of percent rolling for **(A)** Ni$_{49.5}$Ti$_{50.5}$ and **(B)** Ni$_{50.8}$Ti$_{49.2}$ plates.

Results and discussion

Differential scanning calorimetry

The stacked experimental DSC results of four processing conditions (as-received, two intermediate, and potential strain glass states) are presented in Figures 1A,B for Ni$_{49.5}$Ti$_{50.5}$ and Ni$_{50.8}$Ti$_{49.2}$, respectively. The conversion from a sharp single-step martensitic transformation to a continuous strain glass transition as the amount of cold working increased is shown by both alloys. The shift corresponds to the decrease in the enthalpy peak area until the martensitic transformation thermal response is suppressed. For both alloys, the magnitude of the DSC enthalpy peaks decreased with an increased amount of cold rolling and input dislocations. These dislocations induced lattice mismatch and shifted the materials from LRO toward SRO, thus interrupting the characteristic SMA enthalpy peak of the B2→B19′ transformation. An important point to reiterate is that this characterization method does not fully prove that a process-induced SGA was fabricated.

Ni$_{49.5}$Ti$_{50.5}$ was subjected to a 33% cross-sectional reduction before the thermal phase transformation was fully suppressed, as shown in Figure 1A. The intermediate processing samples for this alloy are the 11% and 22% cold-rolled states. Cold rolling from 0% to 11% had the largest reduction in the enthalpy peak area compared to when the sample was further rolled to the 22% and 33% states.

For the Ni$_{50.8}$Ti$_{49.2}$ alloy in Figure 1B, a 24% thickness reduction was required to suppress the enthalpy peak. The intermediate processing samples of this alloy are the 10% and 15% cold-rolled states. A secondary peak is noticed, which is the R phase. The R phase generally arises from the presence of finer grains, which occurs during the cold-rolling process. However, because the resulting potential SGA state has a fixed transformation temperature, the presence of the R phase contributes little to the study. A lower amount of cold rolling was necessary to reach the potential strain glass state for this alloy due to the higher content of Ni compared to the Ni$_{49.5}$Ti$_{50.5}$ alloy.

Transformation temperatures for process-induced SGAs remain fixed, unlike peak shifting, which occurs in compositionally induced SGAs. It is noticed in both alloys that even as the enthalpy peak area

decreases, the hysteresis transformation temperatures are fixed until the potential SGA state, where there is no detected temperature transformation. Because one of the main attributes of SGAs compared to SMAs is the absence of a thermal phase transformation, DSC is often the first method of characterization to indicate potential SGAs and determine the state of transition. However, this characterization method gives no information about the martensitic nanodomains of the material where the fundamental methodology of the strain glass transition occurs.

Vickers hardness

The averaged hardness values and overall trend as the amount of cold rolling increases are shown in Figure 2. As previously stated, the determined SGA mechanical characteristics are dimensional stability, enhanced structural and load-bearing abilities, functional stresses, and recoverability. Vickers hardness testing in this study posed as a rudimentary method to prove a non-linear peak in hardness value at the potential SGA state. There was a relatively linear increase in hardness until the potential SGA state. A peak in hardness was detected at the potential strain glass state, which was 33% for the Ni$_{49.5}$Ti$_{50.5}$ alloy with a value of 455.86 HV. This trend is anticipated, as cold rolling is a method of strain-hardening metals. The alloy was further rolled to the 35% cold-rolled state before it plastically deformed, and a decrease in hardness occurred, falling to 430.46 HV. Peak hardness at the strain glass state is expected because adding dislocations makes a phase transformation difficult and increases the actuation stresses of the alloy, ultimately getting more work out of the alloy. A similar, but less pronounced, trend occurred for the Ni$_{50.8}$Ti$_{49.2}$ alloy, with a peak hardness of 367.38 HV recorded at the 24% state. Further hardness testing beyond the 24% state did not occur due to the alloy cracking when rolled beyond 25%. This clarifies how small the strain glass "window" is and further proves that processing-induced SGAs require a very specific amount of input strain to reach this state.

Further mechanical testing can and should be employed. Specifically, three-point bend testing, uniaxial tensile testing, and dynamic mechanical analysis can generate a more conclusive
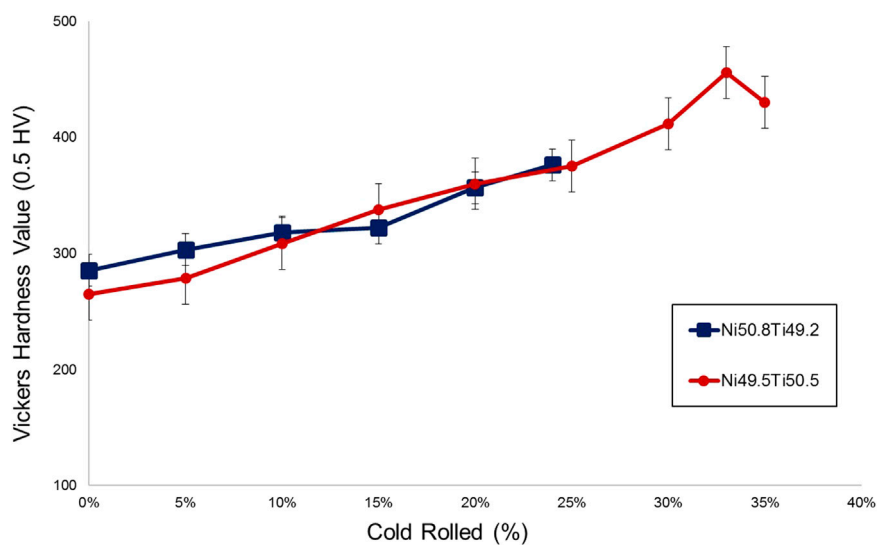
FIGURE 2
Vickers hardness values as a function of percent rolling for $Ni_{49.5}Ti_{50.5}$ and $Ni_{50.8}Ti_{49.2}$.

understanding regarding the thermo-mechanical properties. The previous $Ni_{49.5}Ti_{50.5}$ rod study by Wheeler et al. (2018b) showed the cycling and recoverability capabilities of SGAs when loading and unloading, which were enhanced when compared to the as-received SMA sample. The two considerable mechanical improvements of SGAs compared to SMAs found in this study were: i) SGAs had substantially lower irrecoverable deformation after six loading and stress-free cycles than the SMAs and ii) 60% more energy density from the recoverable transformation was damped out by the SGA compared to the SMA. In this study, both the as-received SMA and the process-induced SGA (at the 45% cold-rolled state) initiated and completed recovery approximately at 70°C and 110°C, respectively. The enhanced thermo-mechanical abilities of SGAs contribute to and explain the core concepts of increased dimensional stability and higher operational stresses when comparing SGAs to SMAs.

Transmission electron microscopy

TEM results present the first nano-characterization method in this study that visualizes the local structures of the samples, that is, the SRO martensitic nanodomains of SGAs compared to the LRO martensitic twins in SMAs. The previous characterization methods, DSC and Vickers hardness, established the necessary amount of cold rolling required to indicate potential SGA states for both alloys. In bright-field TEM, dislocations, as a perturbation of the lattice, scatter the electrons resulting in a lower signal in the region. An increase in dislocations increases the number of scattering centers for conduction electrons, resulting in images appearing darker. A higher density in the deformed areas indicates that it is more difficult for electrons to pass through.

A full depiction of the nanostructure evolution across the top, middle, and bottom of the samples due to input strain is shown in Figures 3A,B and Figures 4A,B for $Ni_{49.5}Ti_{50.5}$ and $Ni_{50.8}Ti_{49.2}$, respectively. For the $Ni_{49.5}Ti_{50.5}$ alloy in Figures 3A,B, the crystalline

martensitic lathes of SMAs versus the amorphous martensitic nanodomains of SGAs are noticed. A variance of nanostructure is observed across the SMA sample, such as twin orientation and a triple point, as shown in Figure 3A. Because this alloy is Ni-lean and martensitic at room temperature, the martensitic twins are visible and give the characteristic microstructure as imaged. Distinct lathes, such as those in Figure 3A (showing the bottom of the SMA sample), measured to be approximately 200 nm in thickness. The lathes noticed in the SMA sample were crushed via cold rolling, resulting in the microstructure present for the SGA shown in Figure 3B. Some lathes from the crystalline matrix are still noticed, such as those seen in Figure 3B, taken from the bottom of the SGA sample, which measured approximately 50 nm–100 nm in length. This is because martensite has both LRO and SRO. However, the fragmented SRO nanodomains are more evident upon further magnification, such as those shown in Figure 3B, which were taken from the middle of the SGA sample.

For the $Ni_{50.8}Ti_{49.2}$ shown in Figures 4A,B, the sample was in the austenitic phase at room temperature, resulting in the presence of large austenitic grains when TEM was conducted. Across the sample shown in Figure 4A, a mixed matrix was present toward the top, and striations appeared from the middle down. For the images from the middle and bottom of the SMA sample, striations were measured to range from 100 nm–400 nm in length. The resulting SGA microstructure in Figure 4B also differed from that in Figure 3B. One reason could be that the sample had to be thinned twice in preparation for TEM imaging because these samples proved to be difficult to mill to the thickness required for TEM. However, with the dominant phase being an austenitic matrix with martensitic nanodomains, a difference in microstructure between the two alloys is expected.

The microstructural transition from crystalline lathes and LRO at the as-received SMA state to nano-sized restricted twins within a crushed matrix of SRO at the SGA state, that is, 33% for $Ni_{49.5}Ti_{50.5}$ and 24% for $Ni_{50.8}Ti_{49.2}$, correlated with the absence of enthalpy peaks from DSC in Figures 1A,B.
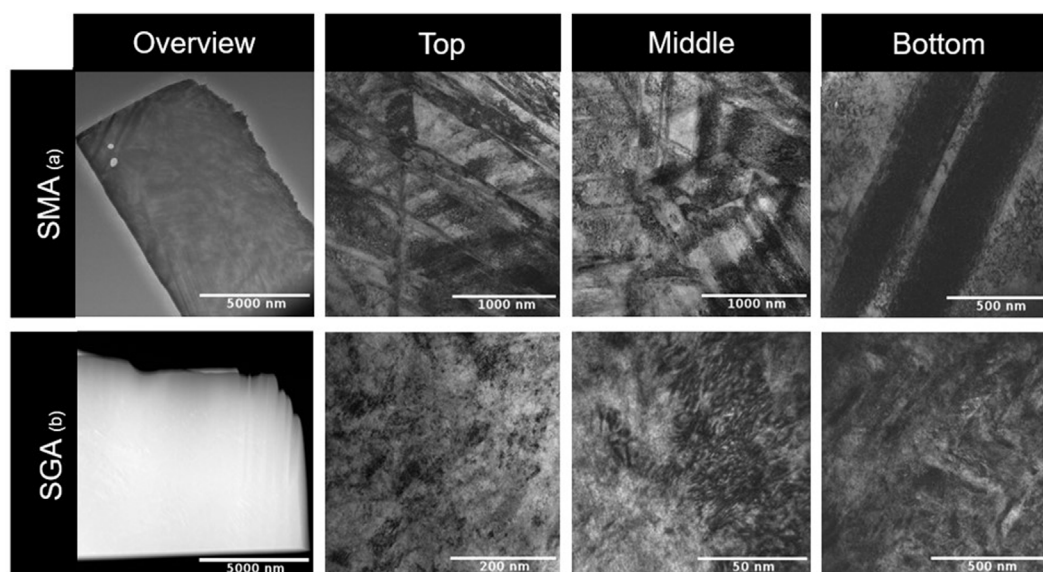
FIGURE 3
Bright-field TEM images from the top, middle, and bottom of the **(A)** SMA (top row) and **(B)** SGA (bottom row) of the $Ni_{49.5}Ti_{50.5}$ plates.

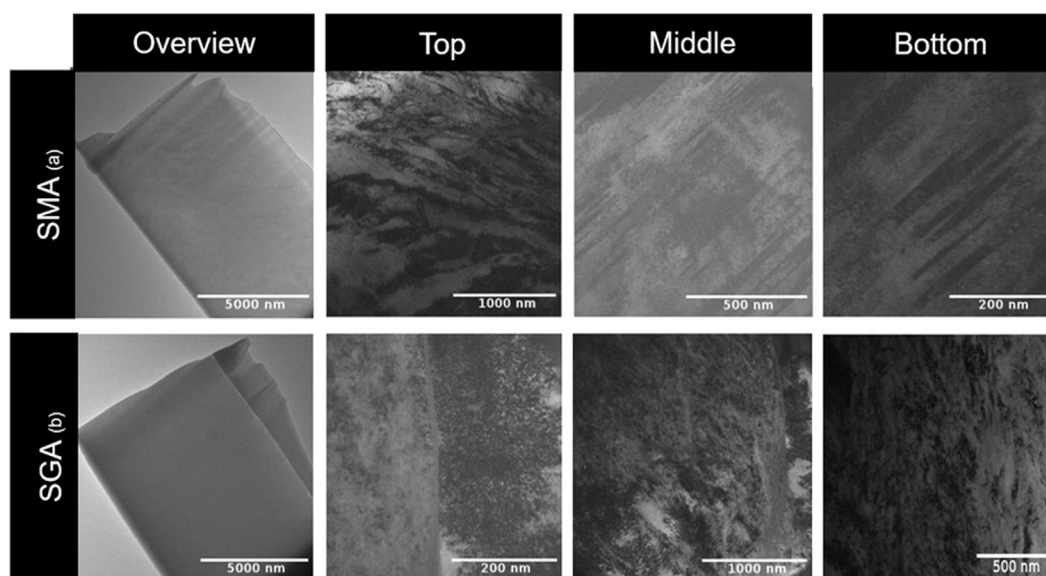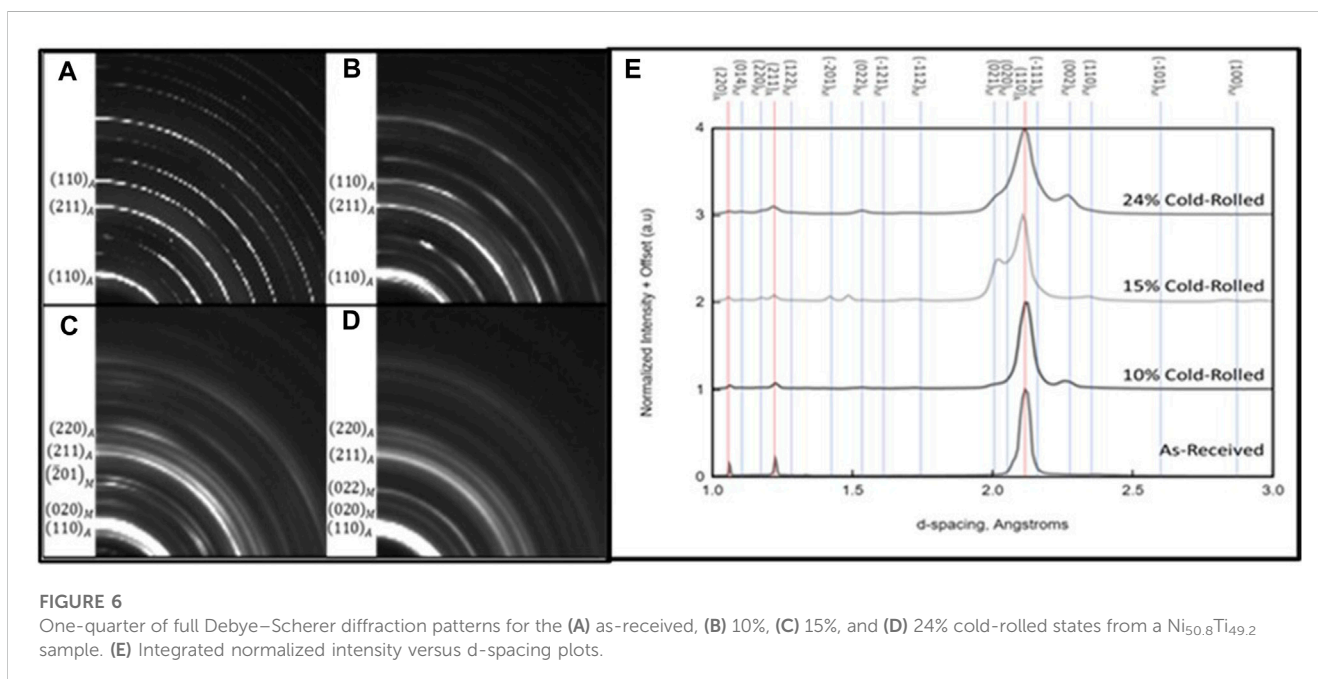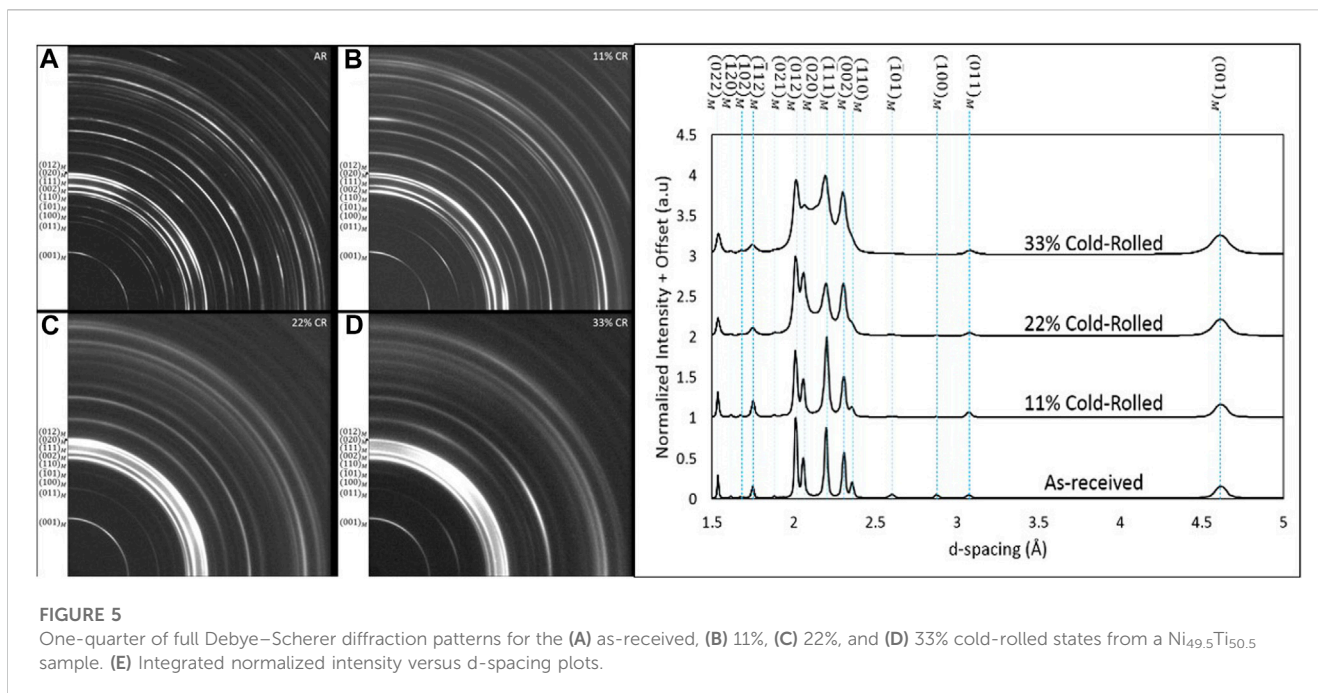**FIGURE 4**
Bright-field TEM images from the top, middle, and bottom of the **(A)** SMA (top row) and **(B)** SGA (bottom row) for the $Ni_{50.8}Ti_{49.2}$ plates.

Synchrotron radiation X-ray diffraction

High-intensity SR-XRD was conducted for the four processing conditions (as-received, two intermediate, and SGA states) in Figures 5A–E and Figures 6A–E for $Ni_{49.5}Ti_{50.5}$ and $Ni_{50.8}Ti_{49.2}$, respectively. The Debye–Scherrer 2D diffraction patterns in Figures 5A–D and Figures 6A–D show a difference in average structure and an increased amount of texturing as a response to the increased amount of input strain from cold working. This indicates that the twins become preferentially oriented. The as-received SMA states in Figure 5A and Figure 6A show relatively untextured and homogeneously distributed microstructure in the diffraction pattern. In comparison, Figure 5D and Figure 6D show the cold-rolled SGA states for $Ni_{49.5}Ti_{50.5}$ and $Ni_{50.8}Ti_{49.2}$, respectively, and it is at this state where the glass-like SRO phase appears. The in-between cold-rolled states, that is, 11% and 22% for $Ni_{49.5}Ti_{50.5}$ and 10% and 15% $Ni_{50.8}Ti_{49.2}$, show the transition states, increased amount of texture, and shift toward strong grain alignment. This was indicated by the nonuniform size and

FIGURE 5
One-quarter of full Debye−Scherer diffraction patterns for the **(A)** as-received, **(B)** 11%, **(C)** 22%, and **(D)** 33% cold-rolled states from a $Ni_{49.5}Ti_{50.5}$ sample. **(E)** Integrated normalized intensity versus d-spacing plots.

FIGURE 6
One-quarter of full Debye−Scherer diffraction patterns for the **(A)** as-received, **(B)** 10%, **(C)** 15%, and **(D)** 24% cold-rolled states from a $Ni_{50.8}Ti_{49.2}$ sample. **(E)** Integrated normalized intensity versus d-spacing plots.

intensity distribution of the diffraction pattern rings. In Figure 5E for $Ni_{49.5}Ti_{50.5}$ and Figure 6E for $Ni_{50.8}Ti_{49.2}$, the glass-like SRO phases from the d-spacing plots show that the peaks became broader as the amount of processing increased. Peak broadening is a common trend from large amounts of applied strain, which results in plastic deformation. It was noticed along the $(111)_M$ and $(001)_M$ for Figure 5E and $(110)_A$ and $(211)_A$ for Figure 6E. This is a standard trend for

transitioning from crystalline states toward more glass-like states. A gradual increase in peak area was observed as the amount of cold rolling increased. This is true and noticed for both $Ni_{49.5}Ti_{50.5}$ and $Ni_{50.8}Ti_{49.2}$ alloys. The large amounts of induced plastic deformation resulted in lattice mismatch and distortion, which were shown by peak broadening and blurring of B2 and B19′ at the SGA state. An increase in peak intensity of the B2 austenitic phase, especially in Figure 5E for $Ni_{49.5}Ti_{50.5}$,
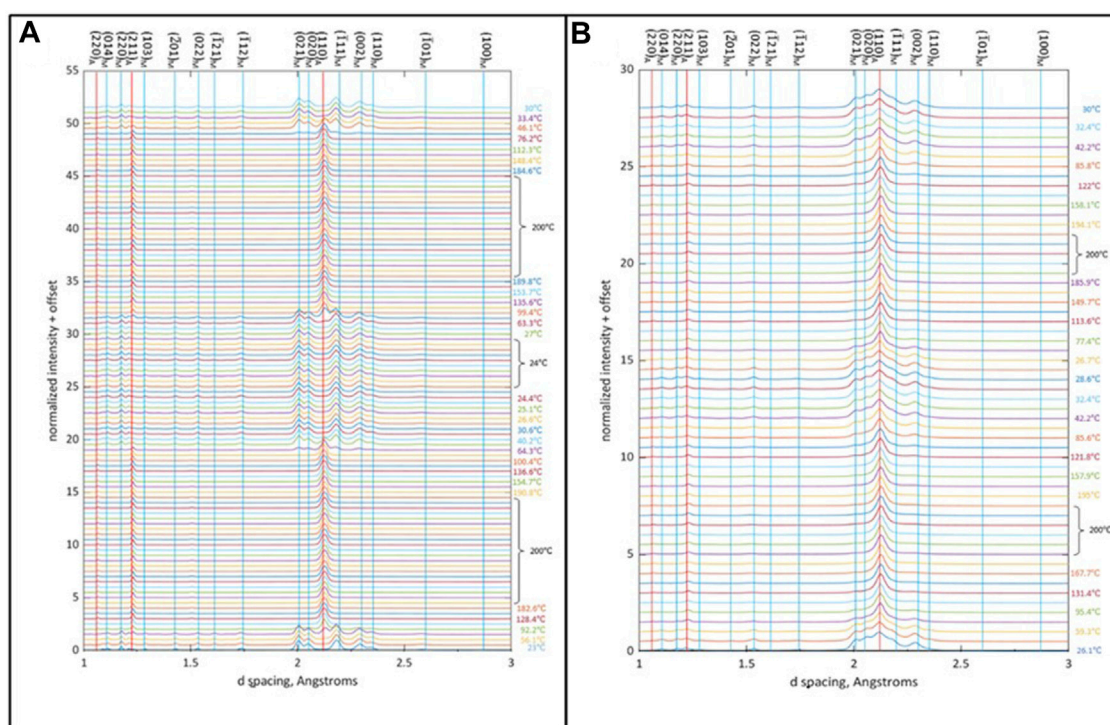
FIGURE 7
Ni$_{49.5}$Ti$_{50.5}$ 1D stacked SR-XRD patterns for the **(A)** as-received SMA and **(B)** cold-worked SGA states. All austenite and martensite (hkl) diffraction planes are labeled on the top.

FIGURE 8
Ni$_{50.8}$Ti$_{49.2}$ 1D stacked SR-XRD patterns for the **(A)** as-received SMA and **(B)** cold-worked SGA states. All austenite and martensite (hkl) diffraction planes are labeled on the top.
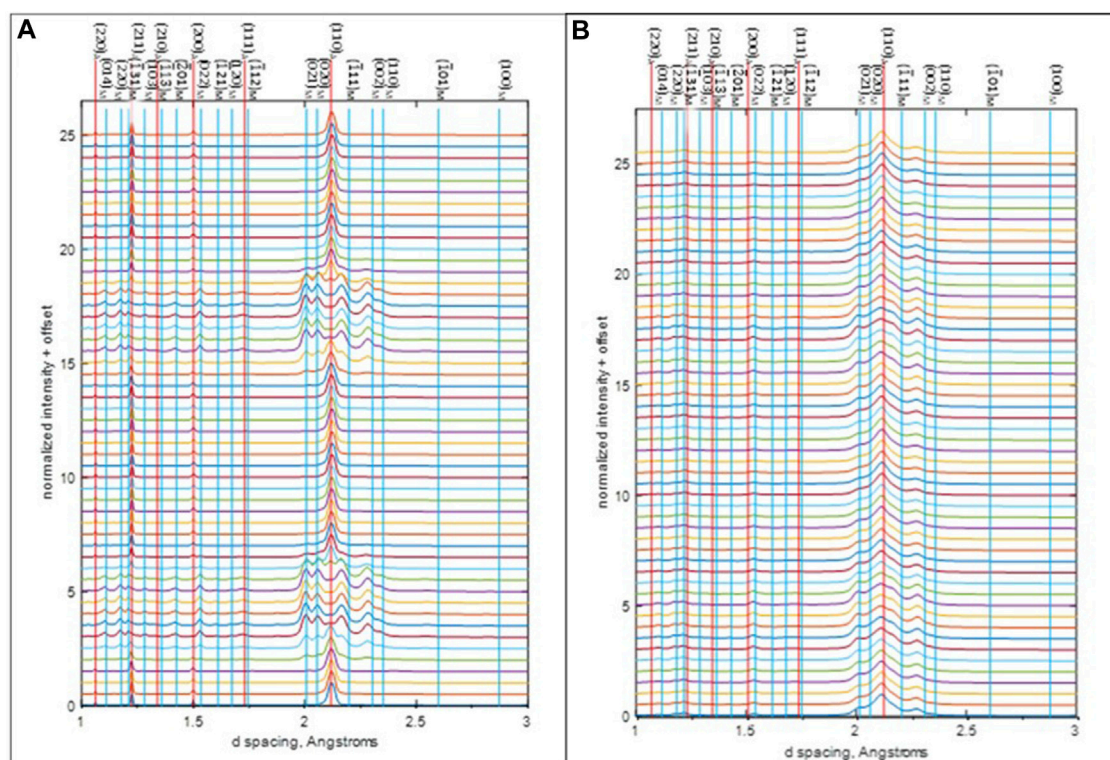
indicated retained austenite with the martensitic phase still present. While peak broadening and blurring alone cannot determine that a transition from crystalline to glass-like states occurred, it is a contributing factor to elucidating the effect of a specific amount of input dislocations on the lattice and the $B2 \rightarrow B19'$ phase transition.

The 1D SR-XRD stacked patterns shown in Figures 7A,B for $Ni_{49.5}Ti_{50.5}$ and in Figures 8A,B for $Ni_{50.8}Ti_{49.2}$ indicate that SGAs are consistent across different temperature profiles and multiple cycles. The cyclical thermal transformation behavior of the as-received SMA and determined SGA states can be correlated to the conducted DSC experiments in Figures 1A,B. It also serves as another visualization of the martensitic transition from being a sharp single step to a continuous transition. The as-received state for $Ni_{49.5}Ti_{50.5}$ shown in Figure 7A displays standard SMA thermal cycling behavior. The full forward transition from martensite to austenite occurs approximately 65°C, confirmed by the appearance of the distinct $(110)_A$ peak. Similarly, the reverse transformation of austenite to martensite occurs at approximately 80°C, which was determined either by the disappearance of the aforementioned $(110)_A$ peak or by the appearance of the $(021)_M$ peak. These transformation temperatures were validated by the DSC data presented in Figure 1A. Similarly, for the $Ni_{50.8}Ti_{49.2}$ SMA state in Figure 8A, the full forward and reverse transformations can be identified by the appearance and disappearance of the $(110)_A$ and $(021)_M$ peaks. In contrast, the SGA states in Figure 7B and Figure 8B have a much less evident phase transformation. These figures provide glimpses of retained austenite and suppressed martensitic phases resulting from the strain glass transition. Retained austenite is evident throughout cycling by the consistent $(110)_A$ peak across heating and cooling cycles. Comparison of the distinct $(021)_M$ peak in the SMA state to the very broad peak in the SGA state proves the suppressed martensitic phase for SGA samples. The observed trends and comparisons between the as-received state and the cold-worked state for both alloys validate the transition from SMA toward the glass-like SGA state via process-induced strain.

Conclusion

A recent method of processing SMAs was utilized to understand the effect of disrupting the martensitic LRO and forming amorphous nanodomains with martensitic SRO. Based on the obtained results, SGA states were analyzed and confirmed using various characterization methods to determine trends and compare $Ni_{49.5}Ti_{50.5}$ and $Ni_{50.8}Ti_{49.2}$. For $Ni_{49.5}Ti_{50.5}$, a 33% thickness reduction was required to obtain a cold work-induced strain glass state, while a 24% reduction was required for $Ni_{50.8}Ti_{49.2}$. This percentage difference is due to the dissimilar amounts of Ni and the resulting parent phase. Various characterization methods provided in-depth analysis and further evaluated the trends for obtaining these strain glass states, as well as the effect of having different parent phases for the starting as-received material.

DSC was the initial characterization method employed to ascertain the amount of cold rolling required for potential SGA states. These potential states were determined by the absence of an enthalpy peak, indicating fixed and constant transformation temperatures. A quintessential characteristic of SGAs is the absence of a thermal phase transformation, which is why DSC tends to be the preliminary characterization method. Vickers hardness testing was conducted to display the enhanced mechanical abilities of potential SGAs compared to SMAs in a straightforward manner. A relatively linear increase with the amount of cold rolling occurs until the SGA state, where the Vickers hardness peaks. The incorporated strain enhances the work output of the material. TEM was the first nano-characterization method to visualize the strain glass transition and verify potential SGA states. A variation in micro-/nano-structure was noticed across the SMA samples, such as lathes, triple points, and striations. Specifically, martensitic twins were noted for the $Ni_{49.5}Ti_{50.5}$ alloy, and large austenitic grains were present for the $Ni_{50.8}Ti_{49.2}$ alloy. A rather consistent profile of martensitic nanodomains is observed across the SGA samples. Different parent phases also resulted in microstructural differences between the two alloys. SR-XRD Debye–Scherrer 2D diffraction patterns further clarified the strain glass transition of these samples based on the increased amount of texture, a shift toward strong grain alignment, and nonuniform size and intensity distribution of the diffraction pattern rings. Peak broadening was a trend noticed for both d-spacing plots and 1D SR-XRD plots and is a common trend for the transition toward more amorphous-like states from a crystalline state; however, it is only a contributing factor for detecting the stain glass transition. The 1D SR-XRD data showed SGAs to be consistent across temperature profiles, which correlated with the obtained DSC data that indicated a retained austenitic phase and a suppressed martensitic phase.

Analysis using these techniques validated the potential strain glass state obtained from DSC and further defined the transition from SMA to SGA using process-induced methods while providing a comparative analysis of using alloys of differing parent phases. The evolution of mechanical ability, microstructure, and crystallographic features was observed under increasing strain.

Data availability statement

The raw data supporting the conclusion of this article will be made available by the authors, without undue reservation.

Author contributions

NJ wrote the manuscript and interpreted the provided data, as well as performed/analyzed DSC and Vickers hardness measurements. BA and RW measured and analyzed SR-XRD data. MW performed and analyzed TEM images. RW provided preliminary research and critical input. MY served as the supervisor of the project, revised the manuscript, and provided critical input. AG was the project funder/supervisor from Army Research Laboratory and provided approval for publication. RW, MY, AG, and NJ contributed to the conception and design of the study. All authors contributed to the article and approved the submitted version.

Funding

Conflict of interest

The authors declare that the research was conducted in the absence of any commercial or financial relationships that could be construed as a potential conflict of interest.

Publisher's note

All claims expressed in this article are solely those of the authors and do not necessarily represent those of their affiliated organizations, or those of the publisher, the editors, and the reviewers. Any product that may be evaluated in this article, or claim that may be made by its manufacturer, is not guaranteed or endorsed by the publisher.

References

Ashmore, B., Young, M. L., and Giri, A. (2023). Synchrotron radiation X-ray diffraction measurements of the thermal response of a processing-induced NiTi strain glass alloy. *Shape Mem. Superelasticity* 9, 87–96. doi:10.1007/s40830-023-00424-2

Bag, P., Chang, P. C., Kuo, Y. K., Wu, S. K., Lin, C., and Li, B. Y. (2019). Coexistence of martensite and strain glass phases in homogenized Ni-rich TiNi shape memory alloys. *Intermet. (Barking)* 109, 16–23. doi:10.1016/j.intermet.2019.03.006

Chang, S.-H., Lin, K.-H., and Wu, S.-K. (2017). Effects of cold-rolling/aging treatments on the shape memory properties of Ti49.3Ni50.7 shape memory alloy. *Mater. (Basel)* 10 (7), 704. doi:10.3390/ma10070704

Chen, C. H., Lu, N. H., Shen, J. J., and Chen, Y. J. (2020). Strain glass and stress-induced martensitic transformation characteristics of Ti40Zr10Ni40Co5Cu5 multi-principal element alloy. *Scr. Mater* 186, 127–131. doi:10.1016/j.scriptamat.2020.04.026

Hao, Y., Ji, Y., Zhang, Z., Yin, M., Liu, C., Zhao, H., et al. (2019). Strain glass in Ti50-x Ni35+x Cu15 shape memory alloys. *Scr. Mater* 168, 71–75. doi:10.1016/j.scriptamat.2019.04.028

Hartl, D. J., and Lagoudas, D. C. (2007). Aerospace applications of shape memory alloys. *Proc. Inst. Mech. Eng. Part G. J. Aerosp. Eng.* 221, 535–552. doi:10.1243/09544100jaero211

Hartl, D. J., and Lagoudas, D. C. (2008). "Thermomechanical characterization of shape memory alloy materials," in *Shape memory alloys* (Cham: Springer). doi:10.1007/978-0-387-47685-8_2

Hou, S. (2012). Evidence for crossover martensite in Ti50Ni45Fe5: An intermediate state between normal martensite and strain glass. *Europhys. Lett.* 100 (5), 58. doi:10.1209/0295-5075/100/58001

Jiang, S., Hu, L., Zhang, Y., and Liang, Y. (2013). Nanocrystallization and amorphization of NiTi shape memory alloy under severe plastic deformation based on local canning compression. *J. Non Cryst. Solids* 367, 23–29. doi:10.1016/j.jnoncrysol.2013.01.051

Kapoor, D. (2017). *Nitinol for medical applications: A brief introduction to the properties and processing of nickel titanium shape memory alloys and their use in stents*, 61. London, United Kingdom: Johnson Matthey Inc.

Khelfaoui, F., and Guénin, G. (2003). Influence of the recovery and recrystallization processes on the martensitic transformation of cold worked equiatomic Ti–Ni alloy. *Mater. Sci. Eng. A* 355, 292–298. doi:10.1016/s0921-5093(03)00068-6

Ko, W. S., Choi, W. S., Xu, G., Choi, P. P., Ikeda, Y., and Grabowski, B. (2021). Dissecting functional degradation in NiTi shape memory alloys containing amorphous regions via atomistic simulations. *Acta Mater* 202, 331–349. doi:10.1016/j.actamat.2020.10.070

Koike, J., Parkin, D. M., and Nastasi, M. (1990). Crystal-to-amorphous transformation of NiTi induced by cold rolling. *J. Mater Res.* 5, 1414–1418. doi:10.1557/jmr.1990.1414

Liang, Q., Zhao, S., Liang, C., Zhao, T., Wang, D., Ding, X., et al. (2022). Strain states and unique properties in cold-rolled TiNi shape memory alloys. *Acta Mater* 231, 117890. doi:10.1016/j.actamat.2022.117890

Lobo, P. S., Almeida, J., and Guerreiro, L. (2015). Shape memory alloys behaviour: A review. *Procedia Eng.* 114, 776–783. doi:10.1016/j.proeng.2015.08.025

Miller, D. A., and Lagoudas, D. C. (2001). Influence of cold work and heat treatment on the shape memory effect and plastic strain development of NiTi. *Mater. Sci. Eng. A* 308, 161–175. doi:10.1016/s0921-5093(00)01982-1

Otsuka, K., and Ren, X. (2005). Physical metallurgy of Ti–Ni-based shape memory alloys. *Prog. Mater Sci.* 50, 511–678. doi:10.1016/j.pmatsci.2004.10.001

Otsuka, K., and Wayman, C. M. (1998). *Shape memory materials*. Cambridge: Cambridge University Press.

Peterlechner, M., Bokeloh, J., Wilde, G., and Waitz, T. (2010). Study of relaxation and crystallization kinetics of NiTi made amorphous by repeated cold rolling. *Acta Mater* 58, 6637–6648. doi:10.1016/j.actamat.2010.08.026

Qin, S. J., Shang, J. X., Wang, F. H., and Chen, Y. (2017). The role of strain glass state in the shape memory alloy Ni50+Ti50–: insight from an atomistic study. *Mater Des.* 120, 238–254. doi:10.1016/j.matdes.2017.02.011

Ren, X. (2011). Strain glass and strain glass transition. *Springer Ser. Mater. Sci.* 148, 201–225. doi:10.1007/978-3-642-20943-7_11

Sarkar, S., Ren, X., and Otsuka, K. (2005). Evidence for strain glass in the ferroelastic-martensitic system Ti50−xNi50+x. *Phys. Rev. Lett.* 95, 205702. doi:10.1103/physrevlett.95.205702

Sergueeva, A. v., Song, C., Valiev, R. Z., and Mukherjee, A. K. (2003). Structure and properties of amorphous and nanocrystalline NiTi prepared by severe plastic deformation and annealing. *Mater. Sci. Eng. A* 339, 159–165. doi:10.1016/S0921-5093(02)00122-3

Stoeckel, D. (1990). Shape memory actuators for automotive applications. *Mater Des.* 11, 302–307. doi:10.1016/0261-3069(90)90013-a

Tadaki, T., Otsuka, K., and Shimizu, K. (1988). Shape memory alloys. *Ann. Rev. Mater. Sci.* 18, 25–45. doi:10.1146/annurev.ms.18.080188.000325

Wang, D., Zhang, Z., Zhang, J., Zhou, Y., Wang, Y., Ding, X., et al. (2010). Strain glass in Fe-doped Ti-Ni. *Acta Mater* 58, 6206–6215. doi:10.1016/j.actamat.2010.07.040

Wang, M., Wang, D., Ji, Y., Ren, X., and Wang, Y. (2022a). Strain glass state, strain glass transition, and controlled strain release. *Annu. Rev. Mater. Res.* 52, 159–187. doi:10.1146/annurev-matsci-081720-091919

Wang, W., Ji, Y., Fang, M., Wang, D., Ren, S., Otsuka, K., et al. (2022b). Reentrant strain glass transition in Ti-Ni-Cu shape memory alloy. *Acta Mater* 226, 117618. doi:10.1016/j.actamat.2022.117618

Wang, Y., Ren, X., and Otsuka, K. (2006). Shape memory effect and superelasticity in a strain glass alloy. *Phys. Rev. Lett.* 97, 225703. doi:10.1103/physrevlett.97.225703

Wheeler, R. W., Lee, C. Y., Ley, N. A., Giri, A., and Young, M. L., (2019). "Processing-induced strain glass alloys in NiTi-based shape memory alloy material systems," in ASM International - International Conference on Shape Memory and Superelastic Technologies, SMST 2019, Konstanz, Germany, 13-17 May 2019.

Wheeler, R. W., Smith, J., Ley, N. A., Giri, A., and Young, M. L. (2018b). Processing-induced strain glass states in a Ni49.5Ti50.5 shape memory alloy. *Appl. Phys. Lett.* 113. doi:10.1063/1.5049871

Wheeler, R. W., Smith, J., Ley, N. A., Giri, A., and Young, M. L. (2018a). "Shape memory behavior of Ni49.5Ti50.5 processing-induced strain glass alloys," in *Minerals, Metals and materials series*. doi:10.1007/978-3-030-05861-6_134

Xu, S., Pons, J., Santamarta, R., Karaman, I., Benafan, O., and Noebe, R. (2021). Strain glass state in Ni-rich Ni-Ti-Zr shape memory alloys. *Acta Mater* 218, 117232. doi:10.1016/j.actamat.2021.117232

Zhang, Z., Wang, Y., Wang, D., Zhou, Y., Otsuka, K., and Ren, X. (2010). Phase diagram of Ti50−xNi50+x: crossover from martensite to strain glass. *Phys. Rev. Lett.* 81, 224102. doi:10.1103/physrevb.81.224102

Zhou, Y., Xue, D., Ding, X., Wang, Y., Zhang, J., Zhang, Z., et al. (2010). Strain glass in doped Ti50(Ni50-xD x) (D = Co, Cr, Mn) alloys: implication for the generality of strain glass in defect-containing ferroelastic systems. *Acta Mater* 58, 5433–5442. doi:10.1016/j.actamat.2010.06.019